Design Procedure for Band-Pass Filters based on Integrated Coaxial and Rectangular Waveguide Resonators

A. A. San-Blas, M. Guglielmi, *Fellow, IEEE,* J. C. Melgarejo,
A. Coves, *Senior Member, IEEE,* and V. E. Boria, *Fellow, IEEE*

Abstract—In this paper, we present a novel band-pass filter based on dual-mode resonators. The dual-mode operation is based on integrated coaxial and rectangular waveguide cavities. Furthermore, we also discuss a systematic design procedure for the selection of the dimensions of the various constituent elements of the filter, that is based on the well-known aggressive space mapping technique. The design of a 5-pole band-pass filter operating in the X-band is discussed in detail, including also measured data. The comparison between simulations and measurement shows very good agreement, thereby fully validating both the new filter structure, and the design procedure.

Index Terms—Band-pass filter, coaxial filter design, comb-line resonator, dual-mode resonators, transmission zeros.

I. INTRODUCTION

THE front end of modern communication satellite payloads is commonly implemented in classical waveguide technology. The evolution of the system architectures constantly requires the ever increasing integration of all waveguide components (such us filters, diplexers and multiplexers) operating in the microwave and millimetre wave frequency ranges. In this context, coaxial cavity filters, based on the comb-line filters initially introduced by Matthaei in 1963 [1], have attracted much attention over the last decades, and are currently widely used both in satellite and in wireless communications systems [2]–[7].

Canonical coaxial filters are usually based on in-line or folded arrangements of single-mode resonators composed of a cylindrical metallic post inside a metallic (cubic) enclosure. The inter-resonator coupling is usually implemented using rectangular irises. Using rectangular irises, both electric and magnetic couplings can be easily implemented by changing the position and height of the iris, as shown in [8]–[11]. Another inter-resonator coupling approach is using electric coupling probes [12], [13]. Folded configurations are usually adopted to enhance the filter selectivity, since they allow the simple realization of cross-couplings between non-adjacent resonators

[11], so that transmission zeros can be implemented. Transmission zeros can also be implemented in in-line configurations by changing the orientation of some of the resonators [14].

Non-canonical coaxial configurations have also been investigated in several contributions. For instance, comb-line resonators with conical posts were described in [15], and comb-line filters with a cellular arrangement were presented in [16], with the aim of implementing diagonal cross-couplings. More recently, in-line coaxial filters using a cylindrical housing were investigated in [17], while novel comb-line resonators adding spheres and half-spheres to the top of the classical cylindrical post were proposed in [18], in order to achieve better power-handling capability. Additionally, mechanically tuned comb-line filters have also been discussed in [19], [20].

Furthermore, several methods have been recently proposed for the efficient design of waveguide coaxial filters. Among them, it is worth noting the investigation discussed in [11], where practical design guidelines are given to compute the initial dimensions of the various irises used in the design of slot coupled comb-line resonators. Another widely used technique for the synthesis of the desired electrical response is based on the construction of the coupling matrix for the whole filter, combined with a direct optimization of the dimensions of the components [10], [11], [21]. More advanced and computationally efficient methods based on space mapping techniques have also been reported in [14], [22]. Furthermore, other design strategies based on the use of equivalent circuits have also been recently proposed [4], [20], [23], [24].

However, little work has been reported so far for the design of comb-line filters based on dual-mode resonators. To the best of the authors' knowledge, the most relevant works in this context are presented in [25], [26], where the canonical comb-line resonator is modified by adding an additional conductor (thus generating another TEM mode), with the aim of implementing dual-mode designs.

In this context, therefore, the objective of this work (which is an extension of our work reported in [27]) is to discuss a novel class of dual-mode band-pass filters based on integrated coaxial and rectangular waveguide resonators. The proposed filter geometry is shown in Fig. 1, where two dual-mode coaxial cavities are combined with an empty rectangular waveguide resonator to obtain a compact design. In contrast to classical coaxial filters, where the comb-line cavities operate in their lowest resonance, the novel resonator uses a higher-order mode resonance of the cylindrical post. The effect of
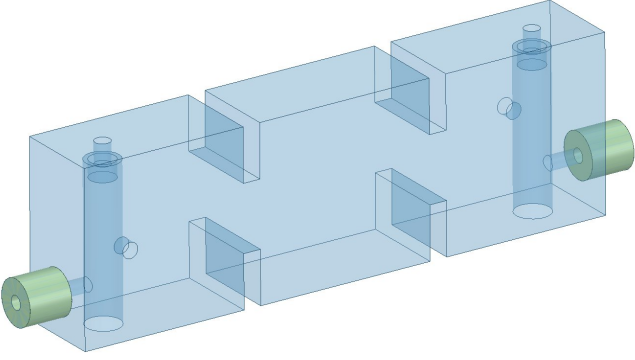
Fig. 1. 5-pole band-pass filter based on dual-mode coaxial resonators proposed in this work.

this choice is that the resonance of the post can be made to coincide with the resonance of the metallic enclosure, thereby generating two orthogonal resonances at the same frequency.

The dual-mode filter that we present is designed following a strategy that combines the segmentation of the component, to better handle the complexity of the structure, with the use of equivalent circuits that provide the desired target performance in each stage of the design process. Furthermore, the well-known aggressive space mapping technique [28] is also used in order to reduce the overall computational effort. The approach that we propose has been validated with the design and manufacture of a fifth-order Chebyshev band-pass filter operating in the X-band ($f_0 = 10$ GHz). The filter has a return loss of 30 dB, and a bandwidth of 300 MHz.

As we stated before, this work is an extended version of the paper that the authors presented in [27]. More specifically, the differences with respect to [27], and the additional topics discussed in this extended version, are described next:

- The authors used in [27] a standard cylindrical post in the dual-mode resonators. In this extended version, we use, instead, a cylindrical re-entrant coaxial post in order to improve the tunability of the filter.
- The two orthogonal modes of the dual-mode cavity designed in [27] were coupled inductively, by means of an auxiliary probe that connected the rectangular enclosure with the cylindrical post. However, this solution does not allow for post-manufacturing tuning of the coupling between the modes of the dual-mode resonator. To improve this aspect, in this extended paper, we propose a new solution based on a capacitively inter-resonator coupling. The new coupling mechanism is fully tunable, thus substantially improving the manufacturability of the structure.
- The design procedure of the band-pass filter is also discussed in more detail in this work, and new material regarding the synthesis procedure of the filter has been included. Moreover, important information about the unloaded Q-factor of the proposed resonator, and its comparison with standard coaxial cavities, are also now included.
- A number of issues of more practical nature, such as the

effect of manufacturing inaccuracies, the introduction of tuning elements and the presence of rounded corners in the resonators, have been discussed as well.
- Another important difference with respect to [27] is that, in this extended work, we also discuss the measured performance of a filter prototype that has been manufactured with the aim of validating both the filter structure and the design procedure.
- Finally, bearing in mind that the filter can be used in future satellite systems, we have also included in this extended version a rigorous multipactor breakdown analysis.

This article is organized as follows. Section II discusses the guidelines for the design of the dual-mode coaxial resonator, while Section III deals with the ideal equivalent network of the filter. Next, a systematic procedure for the efficient design of the filter is discussed in detail in Section IV, where several filter topologies are considered. A multipactor analysis of the filter structure is then performed in Section V. Furthermore, Section VI details the practical implementation of the dual-mode filter. A rigorous tolerance analysis is also performed in Section VII to explain the differences found between the simulated and measured filter response. Next, we discuss in Section VIII the use of the space mapping technique for estimating the depths of the tuning elements used in the filter that we have manufactured. Finally, Section IX summarizes the main results obtained in this work.

II. Design of the dual-mode coaxial cavity

The dual-mode cavity that we propose is based on a cylindrical re-entrant coaxial post in a metallic enclosure, as shown in Fig. 2. It is well known that the use of the re-entrant post increases the capacitance at the open end of the resonator, thereby improving the tunability of the final filter [29]. The design of the dual-mode cavity starts from the identification of the two resonances of interest: one resonance is related to the rectangular waveguide enclosure, while the other is related to the re-entrant coaxial (post) resonator. The modes associated with the two resonances will be coupled afterwards (by means of an electric-type coupling) using an auxiliary cylindrical metallic post.

Our first objective is to obtain the same resonant frequency ($f_0 = 10$ GHz) for both modes. To this aim, the commercial software FEST3D from AuroraSat (now with CST and Dassault Systèmes) and Ansys HFSS are used in the design process. The resonances are identified by finding the zero crossings of the phase of the scattering parameter S_{11} of an appropriate one-port component. In this context, the resonance of the rectangular enclosure can be identified by using an input access port (of rectangular geometry) at $z = 0$ in the resonator shown in Fig. 2. The resonant frequency of the re-entrant coaxial post, on the other hand, can be identified by analyzing the one-port component obtained after considering a coaxial waveguide input port (with a circular inner conductor of diameter $2 R_{p1}$ and a rectangular outer conductor) at $y = 0$ (bottom) in the resonator shown in Fig. 2. For the sake of clarity, the two one-port waveguide components are shown in
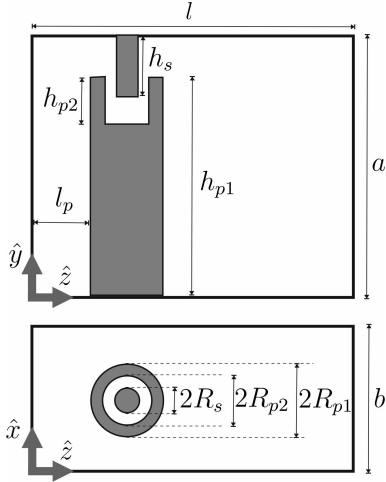
Fig. 2. Re-entrant coaxial resonator in a metallic enclosure. Above: lateral view. Below: top view.

Fig. 5. Design of the resonant frequencies of the dual-mode coaxial cavity using the phase of S_{11}.
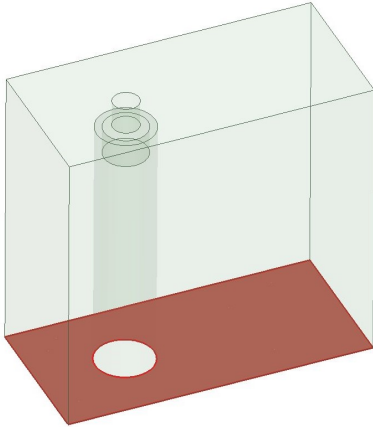

Fig. 3. One-port structure used for computing the resonance of the coaxial resonator.
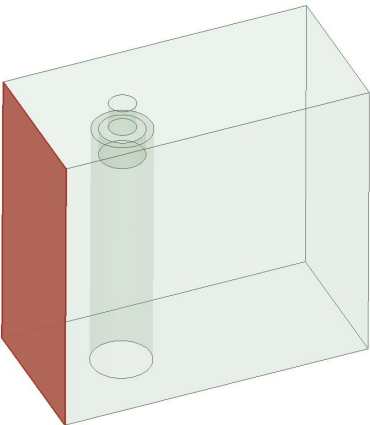

Fig. 4. One-port structure used for computing the resonance of the rectangular enclosure.

Fig. 3 and Fig. 4. In both figures, the corresponding input access ports are shown in red.

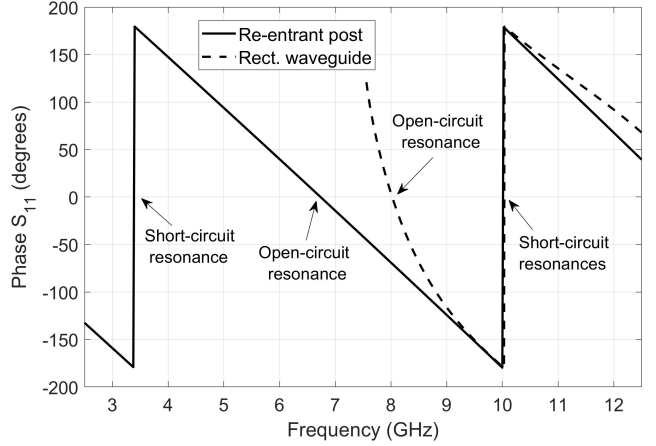It is also important to stress that the transversal dimensions of the input access ports mentioned above are equal to the corresponding transversal dimensions of the cavity used in the filter, so we are not using any external coupling to the resonators themselves. We can simply view them as lengths of waveguides with the appropriate loadings. Therefore, this approach provides us with an approximate (but very good) initial point that can be refined afterwards with an optimization process.

After performing some optimization steps, we obtain the results shown in Fig. 5. It is important to note now that, in order to obtain the same resonant frequency for both resonators, we have chosen to work with the first resonance of the rectangular waveguide enclosure, and with the second resonant mode of the re-entrant coaxial post. The two resonances are orthogonal to each other if no additional coupling structures are introduced in the cavity. It is worth mentioning that, if we had used the first resonance of the coaxial resonator instead of the second one, the post would have been significantly shorter and, as a consequence, we would have needed a very long tuning screw. The result would have been a very impractical structure. Furthermore, if we had tried to reduce the dimension of the rectangular enclosure to reduce the length of the tuning screw, we would have obtained a much smaller rectangular waveguide resonator with a much higher resonant frequency. Dual-mode operation would have, therefore, not been possible. In addition, the choice of working with the second resonance of the post, provides us with a higher unloaded Q, as we will show next.

Fig. 6 and Fig. 7 show the magnitude of the electric field (calculated at 10 GHz) for both resonant modes. Regarding the fields shown in Fig. 7, it is worth noting that they correspond to the first resonance of the rectangular enclosure, perturbed by the presence of the metallic post.

The final dimensions (all in mm) of the dual-mode cavity in Fig. 2 are as follows: $a = 20$, $b = 10$, $l = 20.726$, $h_s = 1.848$, $R_s = 0.9$, $h_{p1} = 18$, $R_{p1} = 2$, $h_{p2} = 2$, $R_{p2} = 1.5$, and $l_p = 4$ (note that h_s, l and l_p will later become optimization variables in the design process).

Next, we have calculated the unloaded Q for the two resonances of the dual-mode cavity, using an equivalent con-
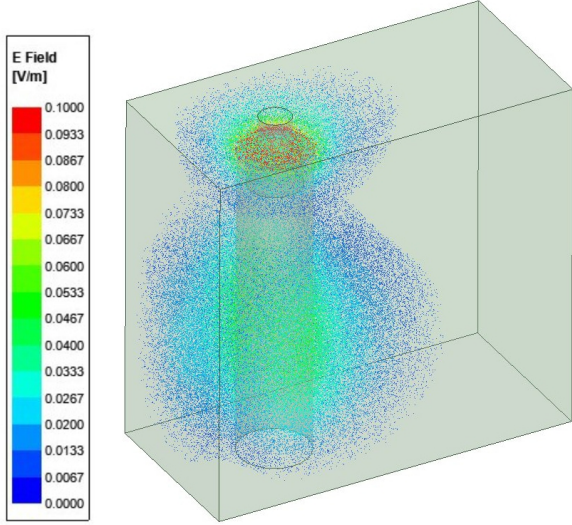
Fig. 6. Magnitude of the electric field (calculated at 10 GHz) for the resonance of the coaxial re-entrant post.
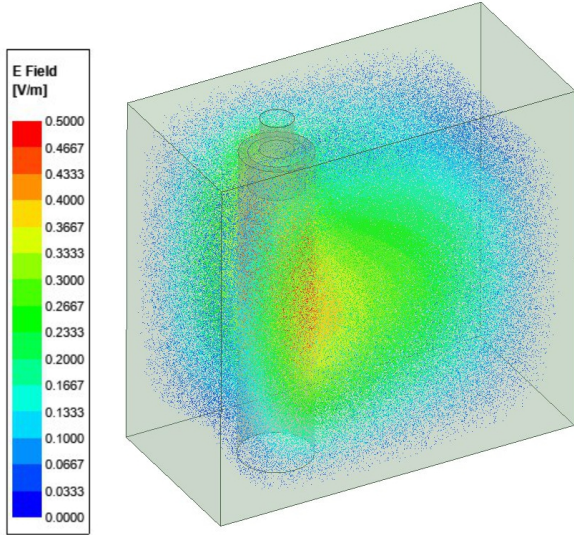

Fig. 7. Magnitude of the electric field (calculated at 10 GHz) for the resonance of the rectangular waveguide resonator.

ductivity value of $38 \cdot 10^6$ S/m (aluminum). To do that, we have used the commercial software Ansys HFSS. The results obtained are collected in Table I. Next, we perform another set of calculations with the aim of comparing the values for the unloaded Q in Table I with the quality factor of an equivalent coaxial cavity that resonates at 10 GHz using the fundamental mode. To achieve this, the height h_{p1} of the post (see Fig. 2) has been reduced to 5.35 mm (i.e., $\lambda_g/5.6$ approximately), while the dimensions of the rectangular enclosure have been kept constant. The unloaded Q factor for the fundamental mode of this coaxial resonator is equal to 2889, which is lower than the Q of the second resonant mode of the coaxial cavity (the one used in our filter).

Finally, in order to compare the performance of the dual-mode cavity with an ordinary comb-line resonator, we

TABLE I
UNLOADED Q OF THE TWO RESONANCES OF THE DUAL-MODE CAVITY

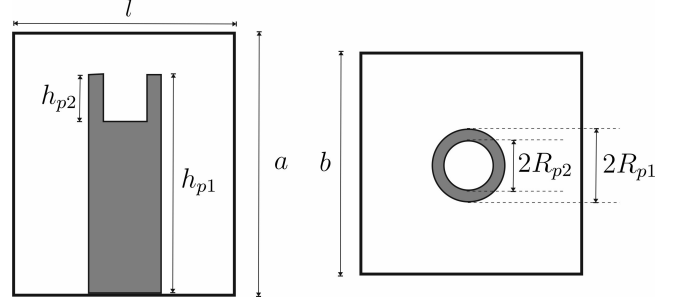| Resonance of the coaxial cavity	$Q=3266$
Resonance of the rectangular enclosure	$Q=4372$

Fig. 8. Geometry of the designed comb-line resonator. Left: lateral view. Right: top view.

have also designed a canonical single-mode comb-line cavity ($f_0 = 10$ GHz), based on a cylindrical re-entrant coaxial post. The geometry of this cavity is shown in Fig. 8. The values (all in mm) of the different dimensions are: $a=8.7$, $b=l=5$, $h_{p1} = 6.59$, $h_{p2} = 1.5$, $R_{p1} = 0.75$, and $R_{p2} = 0.35$. As we expected, although this classical design results in a more compact structure, it cannot be used for dual-mode purposes, since, as already discussed, the resonance of the rectangular enclosure occurs at a much higher frequency than the one of the coaxial resonator we have designed. Furthermore, the values of the unloaded Q factors of the dual-mode cavity (see Table I) are higher than the value for the Q factor of the fundamental mode resonator in Fig. 8, which equals to 1514.

III. EQUIVALENT CIRCUIT OF THE FILTER

We first discuss the equivalent circuit of the dual-mode cavity. The dual-mode resonator is modeled using two coupled resonators. The resonators are represented with a series combination of an inductance and a capacitance, as shown in Fig. 9. The impedance inverter K_{12} represents the electric coupling between the two resonant modes. The slope parameter X related to each resonator at the resonance frequency f_0 is calculated as follows:

$$X = \frac{w_0}{2} \left.\frac{dX_{in}(w)}{dw}\right|_{w=w_0} = Lw_0 \tag{1}$$

where $w_0 = 2\pi f_0$, and X_{in} represents the reactance of the input impedance of the one-port components discussed in the previous section. It is worth noting that, as we pointed out in Section II, there is no need to account for any de-embedding or correcting factor in eq. (1), since we are not using any additional coupling structure at the input ports of the resonators when analyzing the one-port components shown in Fig. 3 and Fig. 4. On the other hand, the value of the capacitance can be readily computed as $C=1/(w_0^2 L)$. Using eq. (1), we can easily obtain the following values for the lumped elements related to the resonance of the re-entrant
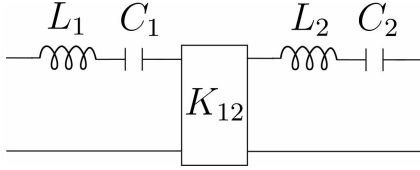
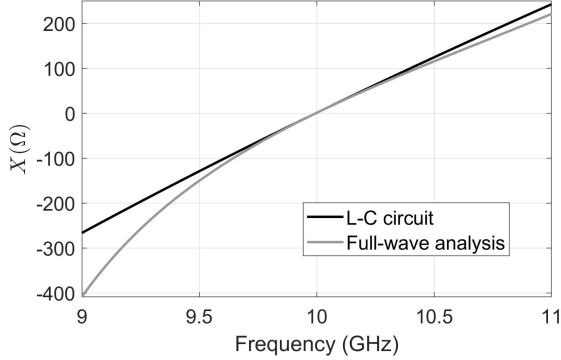Fig. 9. Equivalent circuit of the dual-mode resonator.

Fig. 10. Reactance related to the rectangular waveguide resonator (the enclosure). The reactance computed starting from electromagnetic calculations is compared to the reactance computed with the equivalent circuit.
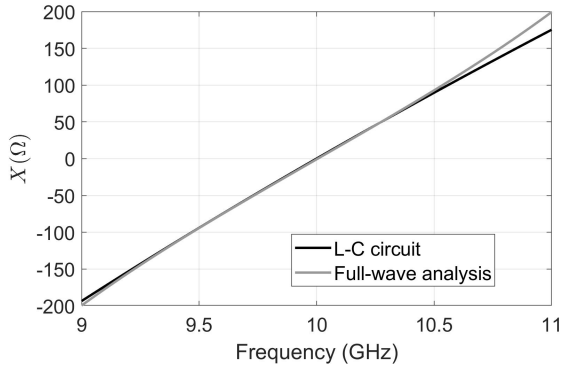

Fig. 11. Reactance related to the coaxial resonator. The reactance computed starting from electromagnetic calculations is compared to the reactance computed with the equivalent circuit.

post: $L_1 = 14.6$ nH, $C_1 = 0.017350$ pF. The values of the inductance and the capacitance for the lumped elements model of the rectangular waveguide resonator are $L_2 = 20.152$ nH and $C_2 = 0.012570$ pF, respectively.

In order to validate the approach that we propose, we have compared (for each resonant mode) the reactance of the L-C equivalent lumped elements resonator with the reactance (calculated with Ansys HFSS) of the corresponding one-port waveguide component. The results that we obtain are shown in Fig. 10 and Fig. 11, where a very good agreement between both type of results can be observed for each mode, especially around the central frequency (10 GHz) of the filter pass-band. We can, therefore, conclude that our simple equivalent circuits do represent very accurately both resonators in the vicinity of their resonant frequencies.
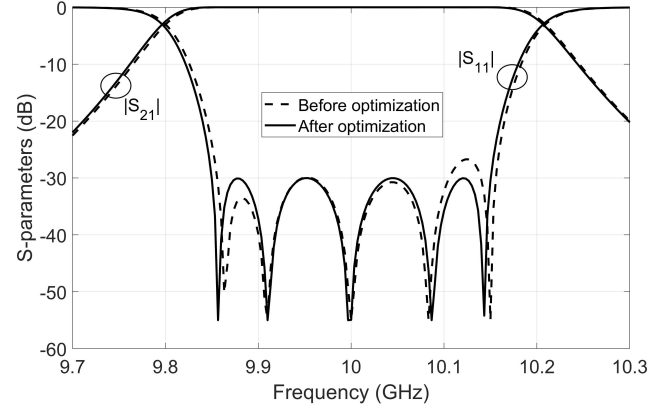

Fig. 12. Electrical response of the equivalent circuit of the filter.

The equivalent circuit of the complete filter is finally assembled using a hybrid network that combines lumped and distributed elements. In addition to the L-C series network used for each dual-mode cavity, a transmission line of length $\lambda_g/2 = 22.642$ mm is, in fact, used to represent the empty rectangular waveguide resonator placed in the center of the filter (see Fig. 1). The input and output couplings, as well as the inter-resonator couplings, are modeled by ideal impedance inverters. The values of the inverters are computed using the slope parameters of the resonators [30]. In particular, we obtain the following values (all in ohms, Ω) for the given specifications: $K_{01} = 103.631$, $K_{12} = 35.509$, and $K_{23} = 35.606$ (note that $K_{34} = K_{23}$, $K_{45} = K_{12}$ and $K_{56} = K_{01}$).

The electrical response of the equivalent circuit of the filter is shown in Fig. 12 with a dotted line, where a slightly non-equiripple pass-band response can be observed. This problem is due to the waveguide dispersion effect. Although a similar approach for obtaining the equivalent circuit of a 5-pole inductive filter (whose pass-band was also centered at 10 GHz) was used by the authors in [27], the width of the central waveguide of the filter designed in [27] was greater than the dimension used in this design, thus decreasing the waveguide dispersion near the pass-band so that an equiripple response was obtained directly without any further work.

A simple optimization procedure of the values of the impedance inverters and the resonant frequencies of the cavities can, however, easily recover the equiripple response. In the optimization, we have assumed that, in the dual-mode cavity, the slope parameters related to both modes remain unchanged, so that only the values of the equivalent capacitance are optimized. After performing the optimization, the following values (all in ohms, Ω) are obtained for the ideal impedance inverters: $K_{01} = 103.761$, $K_{12} = 35.631$, and $K_{23} = 35.721$. The new optimized values for the capacitances of the L-C series network (dual-mode cavity) are $C_1 = 0.017353$ pF and $C_2 = 0.012576$ pF, while the new length of the transmission line that represents the rectangular waveguide resonator is 22.662 mm. In Fig. 12, we have also included (using a solid line) the electrical response of the equivalent circuit of the filter after the optimization. As we can see, a perfectly equiripple response has been finally obtained. There is, however, a very
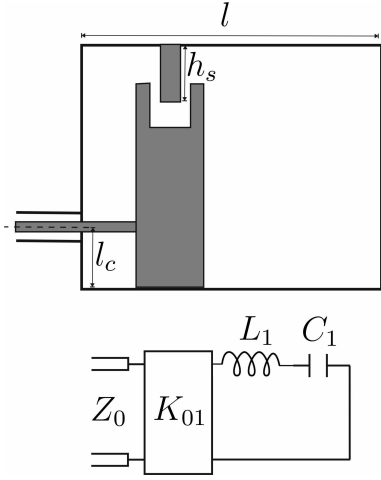
Fig. 13. Waveguide component used for designing the coaxial feeding (top), and the relevant equivalent circuit (bottom).

Fig. 14. Results of the optimization process after designing the coaxial feeding.

slight frequency shift in the equiripple response due to the optimization of the resonant frequencies of the resonators.

IV. DESIGN OF THE DUAL-MODE COAXIAL FILTER

In this section, we describe a systematic and efficient design procedure for the dual-mode coaxial filter that we propose. The design process is decomposed into a number of simple stages. This is done in order to minimize the number of variables to be optimized in each step [23], [27]. In addition, the electrical response of an appropriate equivalent circuit will be used in each stage as a target response. It is also important to mention that the well-known aggressive space mapping technique [28] will be used in order to reduce the computational effort, while guaranteeing the accuracy of the final results. In this context, therefore, the commercial software tool FEST3D will be used as the coarse model, while the finite-element tool Ansys HFSS will be used as the accurate model.

A. Design of the coaxial input and output ports

The input and output ports of the filter are implemented using a $50\,\Omega$ commercial coaxial connector ($r_{out} = 2.625$ mm, $r_{in} = 0.82$ mm, $\epsilon_r = 2.1$). The inner conductor of the coaxial line is in contact with the re-entrant post. The first step of the design process consists of obtaining the height l_c of the input coaxial connection. To this aim, a coaxial waveguide input port is included in the dual-mode cavity designed in Section II, as shown in Fig. 13. The equivalent circuit of this component is also represented in Fig. 13.

Next, the electrical response of the input arrangement is optimized considering the group delay of the S_{11} parameter of the equivalent network as the target response (the variables to be optimized are indicated in Fig. 13). The results of the optimization are shown in Fig. 14, where we can see a very good agreement between the various results. The optimized values of the structure are (see Fig. 13): $h_s = 2.739$ mm, $l = 20.595$ mm and $l_c = 5.283$ mm.
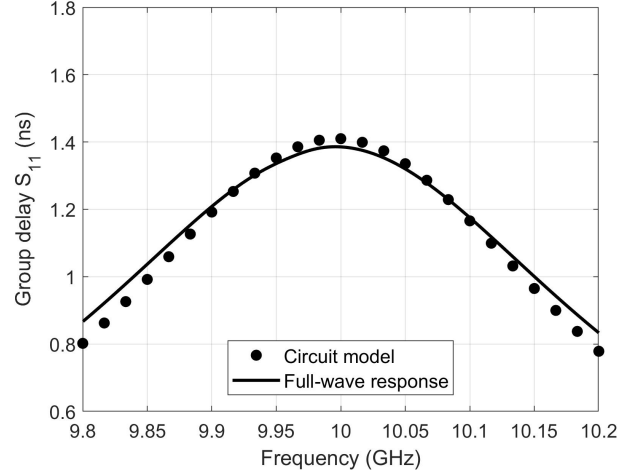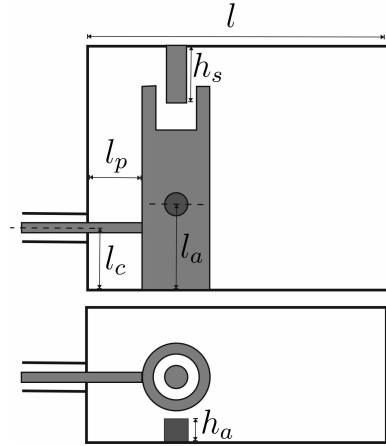

Fig. 15. Waveguide component used for analyzing the electromagnetic coupling between the two resonances of the dual-mode cavity.

B. Design of the electric coupling between the modes of the dual-mode resonator

The two resonances of the dual-mode cavity are capacitively coupled by means of an auxiliary cylindrical post of height h_a, as shown in Fig. 15 (the radius of the post is 0.9 mm). It is important to recall that, in contrast to the strategy used in our previous work [27], where the two modes of the resonator were coupled inductively, we now use an electric coupling in order to be able to tune the coupling value after manufacturing.

In Fig. 16 and Fig. 17, we show the coupling between the two modes of the dual-mode resonator, when a capacitive coupling is used. In particular, Fig. 16 shows the coupling calculated in terms of the height h_a of the post (the offset of the post has been set to $l_a = 8$ mm). Considering the fact that the electromagnetic coupling that is required between the two resonances is $k_{12} = K_{12}/\sqrt{X_1 X_2} = 0.03306$, a good starting point is found to be $h_a = 1.565$ mm. On the other hand, Fig. 17 shows the coupling obtained in terms of the offset l_a of the post (this time, the height of the post has been set to $h_a = 1.565$ mm). As we can see, the coupling between the
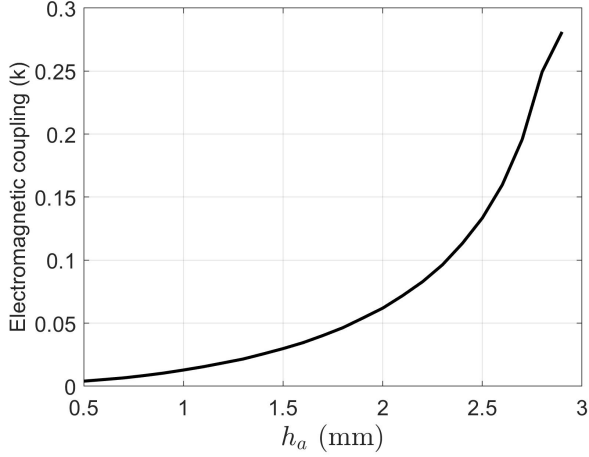
Fig. 16. Coupling between the modes of the dual-mode cavity in terms of the height of the post (fixing $l_a = 8$ mm).
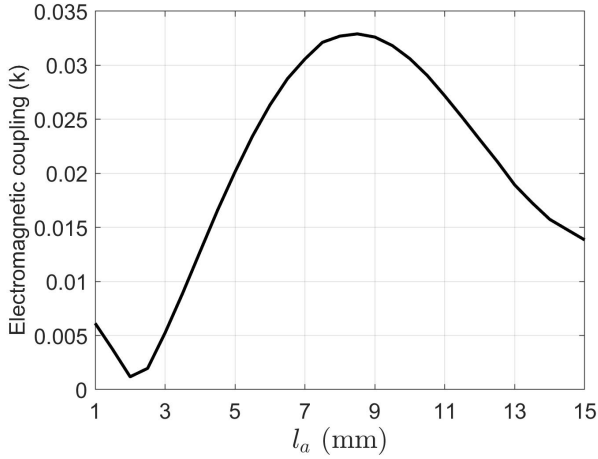

Fig. 17. Coupling between the modes of the dual-mode cavity in terms of the offset of the post (fixing $h_a = 1.565$ mm).

two modes depends mostly on the height h_a of the post, and a wide range of coupling coefficients can be achieved. The coupling also depends, to a lesser extent, on the offset l_a, as shown in Fig. 17.

On the other hand, Fig. 18 shows the inter-resonator coupling (in terms of the offset l_a) obtained with an inductive coupling. In this case (as it was done in [27]), an auxiliary cylindrical probe of radius 0.5 mm is used to connect the rectangular enclosure with the re-entrant post. Although a wide range of coupling values can also be achieved with this approach, an important disadvantage of this solution (as we have already mentioned before) is the impossibility to tune manually the coupling value after the filter is manufactured. For this reason, in the remainder of the paper we will use the capacitive inter-resonator coupling.

Next, a new optimization is performed using the waveguide component shown in Fig. 15. The initial dimensions of this structure have been derived in the previous design stages. The objective is to optimize the group delay of the S_{11} parameter
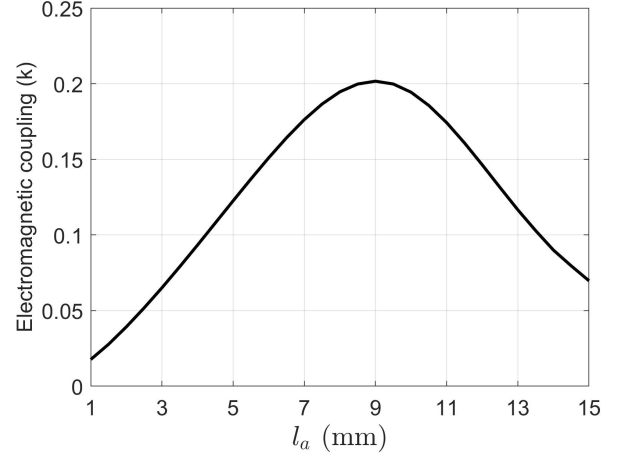

Fig. 18. Inter-resonator coupling using an inductive coupling (through an auxiliary cylindrical connecting probe of radius 0.5 mm).
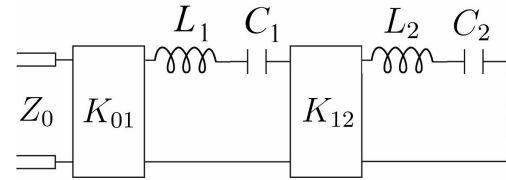
Fig. 19. Ideal network representing the waveguide component shown in Fig. 15.
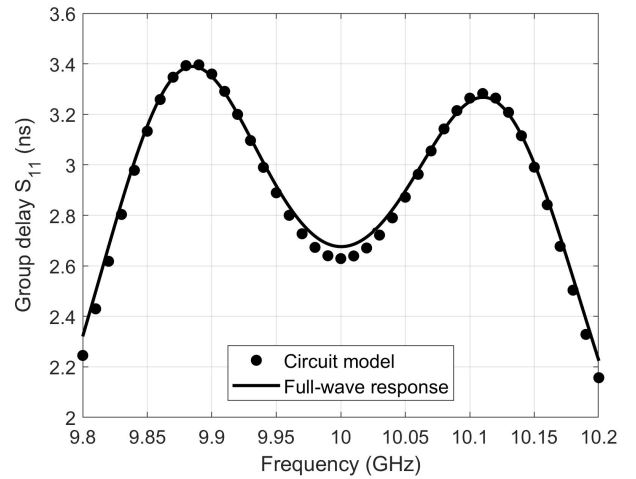
Fig. 20. Results of the optimization process for the coupling between the two modes of the dual-mode resonator.

of the waveguide component, using as a target the response of the ideal network in Fig. 19. The dimensions to be optimized in this stage are defined in Fig. 15. The results of the optimization are shown in Fig. 20. As we can see, a very good agreement between the results has again been obtained. The values (all in mm) of the optimized dimensions are (see Fig. 15): $h_a = 1.6$, $h_s = 2.461$, $l = 20.005$, $l_a = 8.399$, $l_c = 4.601$ and $l_p = 3.611$.

Fig. 21. Waveguide component (and its equivalent ideal network) used for the design of the coupling between the dual-mode resonator and the empty cavity.

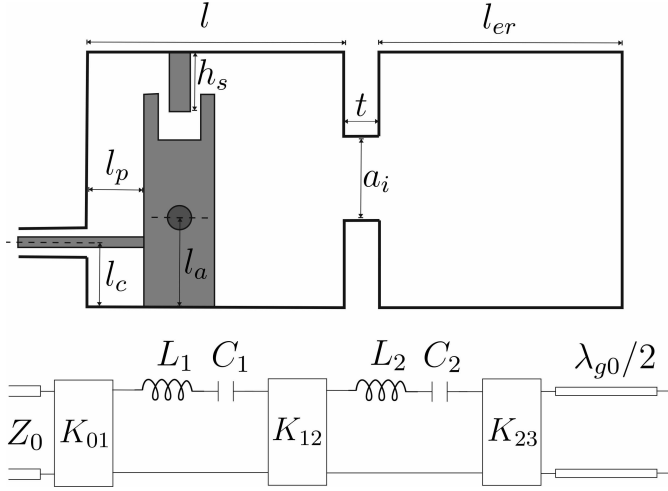Fig. 22. Results of the optimization process after designing the coupling between the dual-mode resonator and the empty cavity.

C. Coupling the dual-mode cavity to the rectangular waveguide resonator

In the next stage of the design process, the rectangular waveguide resonator is added to the structure. The additional resonator is coupled to the dual-mode cavity with a rectangular iris. Fig. 21 shows the waveguide component to be considered in this step, and the corresponding ideal equivalent network.

The height of the iris is equal to b (that is, the same height as the resonators), while its thickness t is set at 2.5 mm. Furthermore, the length l_{er} of the empty resonator is initially set at 22.66 mm, in order to get a resonance at f_0.

First of all, we are interested in obtaining an initial value for the width a_i of the iris. With this aim, the electromagnetic coupling between the empty cavity and the dual-mode cavity is computed in terms of the width of the iris. The waveguide structure in Fig. 21 can be used for this purpose, after removing the auxiliary post and considering directly, as input and output ports, the rectangular waveguide to the left and to the right of the iris, respectively. Given the fact that the required coupling is $k_{23} = K_{23}/\sqrt{X_2 X_{er}} = 0.02223$ (where X_2 represents the slope parameter of the resonance related to the rectangular waveguide of the dual-mode cavity, and X_{er} denotes the slope parameter of the empty resonator), the value that we obtain is $a_i = 6.75$ mm.

Next, the dimensions of the waveguide component shown in Fig. 21 are optimized considering the electrical response of its equivalent network as the target function. The result obtained is shown in Fig. 22. The final values (all in mm) for the optimized dimensions are: $a_i = 7.644$, $h_a = 1.602$, $h_s = 2.556$, $l = 19.188$, $l_a = 9.799$, $l_c = 4.793$, $l_{er} = 21.509$ and $l_p = 3.476$.

D. Design of the complete filter

At this stage, we have the starting dimensions for the complete filter since the component is symmetrical. Fig. 23 shows the top view of the structure. The dimensions obtained in the previous stages are now going to be used as an initial
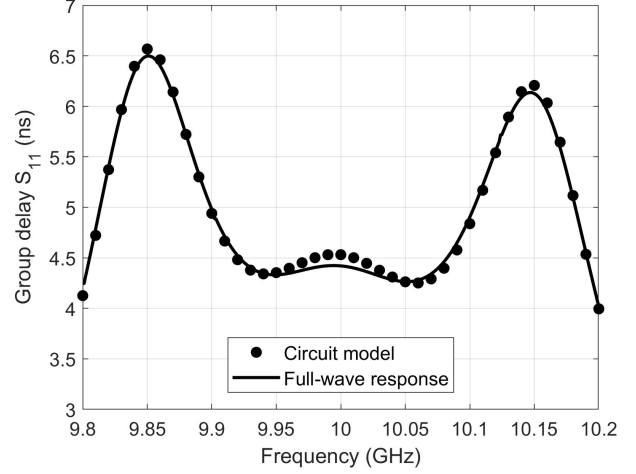

Fig. 23. Top view of the complete dual-mode coaxial filter.

point for the final optimization of the complete filter. The ideal network of the filter can be easily obtained starting from the network shown in Fig. 21, after eliminating the short-circuit at the end of the transmission line, and replicating symmetrically the rest of the inverters and lumped elements resonators. The magnitude of S_{11} and S_{21} obtained from this ideal network (see Fig. 12), will be used as the target function for the optimization.

Fig. 24 shows the results of the optimization process, where an excellent agreement between both data set can be observed. The dimensions (all in mm) of the filter are (the notation used for the different variables can be found in Fig. 15 and Fig. 21): $a_i = 7.663$, $h_a = 1.6$, $h_s = 2.547$, $l = 19.143$, $l_a = 9.75$, $l_c = 4.771$, $l_{er} = 20.396$ and $l_p = 3.501$. It is also important to note that the final dimensions of the component are very close to those that we have derived in the previous stages of the design process, thus fully validating our design methodology.

The out-of-band performance of the filter is shown in Fig. 25. As we can see, there is a transmission zero in the lower side of the pass-band. The transmission zero is located to the left of the pass-band due to the capacitive coupling implemented between the two modes of the dual-mode cavity. Transmission zeros are normally used to improve the selectivity of the designed filter. In this case, however, this improvement is not very significant, if we compare the out-of-band response of our filter with the performance of the corresponding ideal response. Furthermore, the frequency location of this transmission zero cannot be controlled independently from the rest of the filter characteristics. It is, however, true
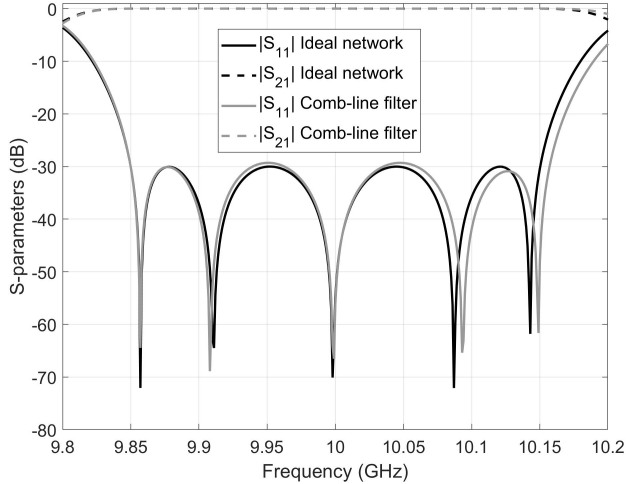
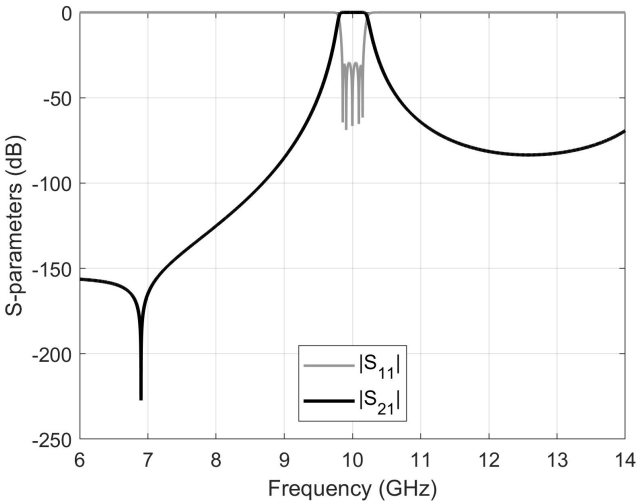Fig. 24. Electrical response of the dual-mode coaxial filter compared to the response of the ideal network.

Fig. 25. Out-of-band performance of the dual-mode filter.

Fig. 26. Dual-mode coaxial filter with tuning screws and rounded corners in the cavities.

that the location of the zero is affected by the offset l_a of the coupling post, but this effect is, indeed, very small. In practice, therefore, the frequency location of the transmission zero must be accepted as is. It is also worth noting that, if we had used an inductive inter-resonator coupling (as the authors did in [27]), the transmission zero would have been located in the upper side of the pass-band.

Compared to classical inductive waveguide filters, this solution provides us with a significantly more compact design, since the coaxial excitation of the filter is integrated in the first resonator and dual-mode cavities are used.

E. Consideration of mechanization effects

To manufacture the filter, we will use a standard, low-cost milling technique. As a consequence, we now need to account for the introduction of rounded corners in the cavities of the device. Furthermore, since the manufacturing accuracy
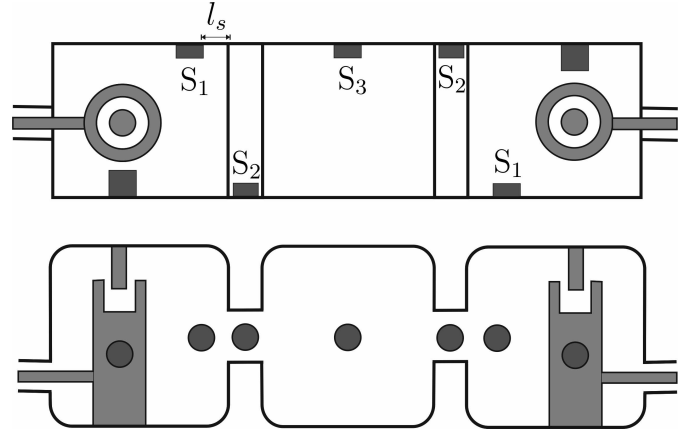
of standard milling is limited, we will also use cylindrical tuning elements to compensate for the manufacturing errors.

In Fig. 26, we show the modified geometry of the filter that includes the rounded corners in the cavities, and several cylindrical tuning elements (S_1, S_2 and S_3). The radius of the rounded corners is set at 2 mm, while the radius and depth of the tuning screws are set at 0.9 and 1.0 mm, respectively. The tuning screws S_1 control the resonance of the rectangular waveguide cavity in the dual-mode resonator. The resonance of the post in the dual-mode cavity is controlled by the tuner at the top of the re-entrant post itself. The tuner S_2 is placed at the center of the iris to control the inter-resonator coupling, while the tuning element S_3 (placed at the center of the central empty cavity) controls the resonance of the empty rectangular waveguide resonator.

In order to proceed with the design, we will now segment the filter designed in the previous section into the following two blocks that will be optimized separately:

1) A dual-mode cavity fed on one side by the coaxial input port, and with the opposite side coupled by an inductive iris to a rectangular waveguide (the output).
2) An empty resonator with rectangular waveguide input and output ports (the central rectangular waveguide cavity) with inductive input and output irises.

The first step is to compute the ideal response of the two separate blocks in order to obtain the desired target functions. Next, the rounded corners are introduced in the dual-mode cavity described in 1). After that, all dimensions are re-optimized to recover the corresponding target response. Next, the different tuning elements are added progressively to the structure, and an optimization is carried out for each step. An identical design strategy is then followed with the component described in 2). Finally, the whole filter is assembled and a final optimization is performed.

The results obtained are shown in Fig. 27, where an excellent agreement is observed between the ideal and the *real* result. The dimensions (all in mm) of the filter are (see Fig. 15 Fig. 21, and Fig. 26): $a_i = 8.148$, $h_a = 1.704$, $h_s = 2.591$, $l = 19.001$, $l_a = 10.1$, $l_c = 4.769$, $l_{er} = 19.972$, $l_p = 3.236$ and $l_s = 4.143$.
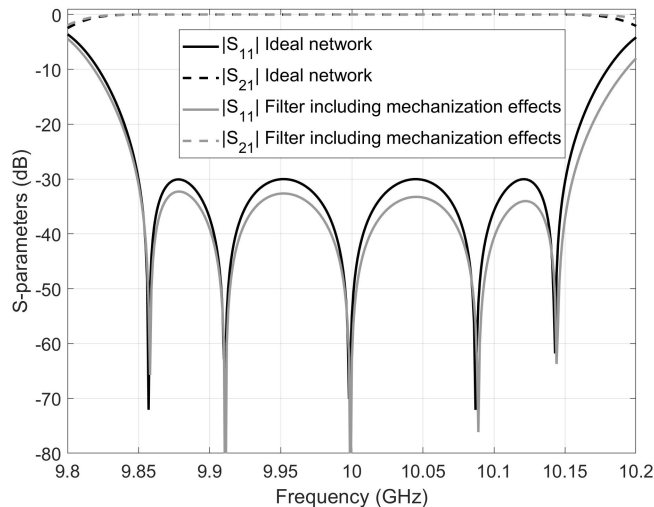
Fig. 27. In-band electrical response of the dual-mode coaxial filter after including rounded corners in the cavities and several tuning screws.

Fig. 28. Implementation of the aggressive space mapping technique to recover the electrical response of the filter designed in the coarse space.

F. Implementation of the space mapping technique

The design process discussed in the previous sections has been carried out using FEST3D with a set of computational parameters chosen to have an efficient simulation. With the set of parameter chosen, however, the result produced by FEST3D is not adequate for manufacturing (not accurate enough). In this section, we therefore discuss the implementation of the well-known aggressive space mapping (ASM) technique [28], in order to obtain accurate dimensions that can be used to manufacture the filter. As it is well-known, ASM employs two different simulation spaces: a low accuracy space (or coarse model) and a high accuracy space (or fine model). ASM technique is efficient because most of the simulations are performed in the coarse space, while the fine space is used only for validation.

In Fig. 28, we show the results after implementing the ASM technique. All the simulations performed in the high accuracy space have been carried out using the commercial software Ansys HFSS, while FEST3D has been used to generate the results in the coarse space. With only 3 iterations, we have been able to recover almost exactly the electrical response of the filter designed in Section IV-E (coarse space response). The final dimensions (all in mm) of the filter are: $a_i = 8.092$, $h_a = 1.697$, $h_s = 2.515$, $l = 18.821$, $l_a = 9.956$, $l_c = 4.801$, $l_{er} = 19.798$, $l_p = 3.236$ and $l_s = 3.975$. Finally, Fig. 29 shows the broadband response of the filter calculated with Ansys HFSS.

G. Coaxial filter topology with mixed inter-resonator couplings

In this section, we discuss the design of another 5-pole Chebyshev band-pass filter (centred again at $f_0 = 10$ GHz and with 20 dB of return loss) with both inductive and capacitive inter-resonator couplings. The topology of the filter (see Fig. 30), is very similar to the filter structure discussed up
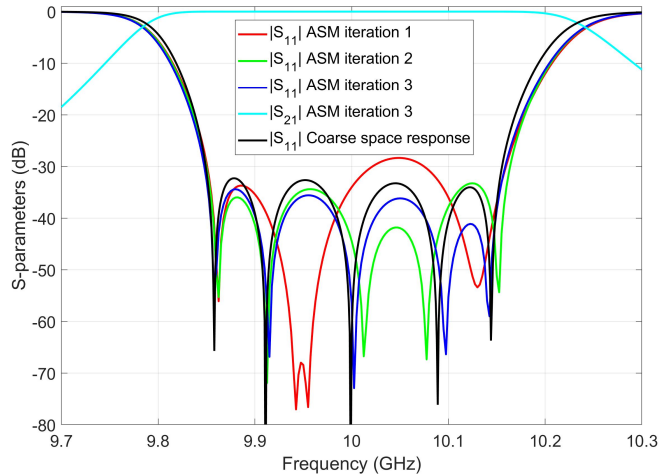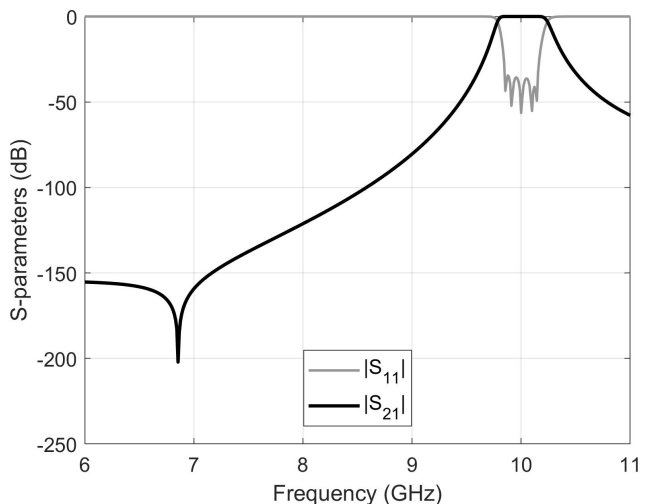

Fig. 29. Out-of-band response of the filter shown in Fig. 26 calculated with Ansys HFSS.

to now. The main difference is that, in the second dual-mode resonator, the inter-resonator coupling is implemented with an auxiliary probe that connects the side wall of the rectangular waveguide enclosure to the cylindrical post, thus implementing an inductive coupling between the two modes of the resonator [27]. A further difference is that a standard cylindrical post (instead of a re-entrant post) is used in both dual-mode cavities of this filter example.

The dimensions of the filter have been synthesized using the same design strategy discussed in the previous sections. The broadband frequency response of this new filter is shown in Fig. 31, where two transmission zeros are clearly visible at 8 and 12.9 GHz. The final dimensions of the filter are given in Table II.

Finally, it is worth noting that, although this topology is able to implement two transmission zeros, the authors have decided

Fig. 30. Band-pass filter combining two dual-mode coaxial resonators with electric and magnetic couplings.

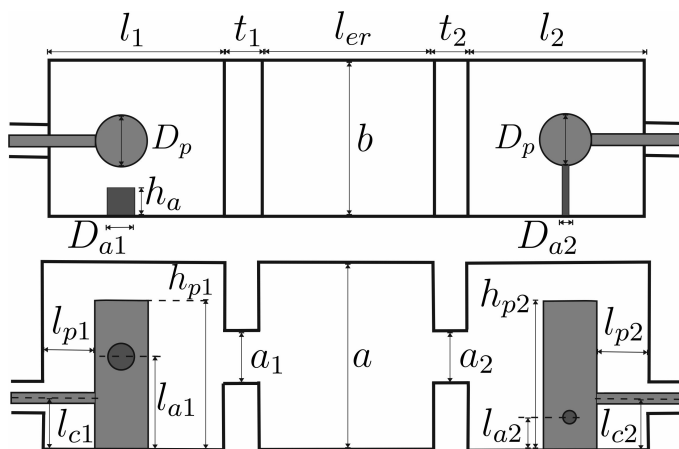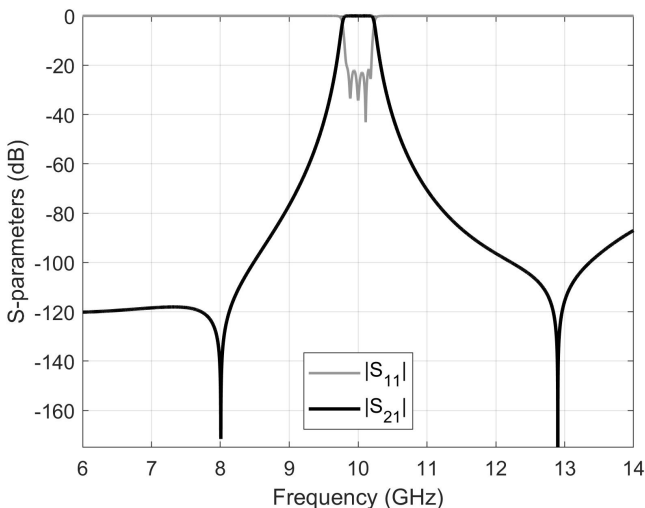| Dimensions	Value (mm)
a, b	25.0, 10.0
l_1, l_2, l_{er}	14.495, 15.957, 17.199
t_1, t_2	2.234, 2.043
a_1, a_2	7.255, 7.150
h_a, D_{a1}, l_{a1}	1.531, 2.246, 11.938
D_{a2}, l_{a2}	1.0, 2.431
D_p, h_{p1}, h_{p2}	4.0, 21.616, 21.948
l_{c1}, l_{p1}	7.048, 4.669
l_{c2}, l_{p2}	5.158, 4.170

Fig. 31. Out-of-band performance of the dual-mode band-pass filter shown in Fig. 30.
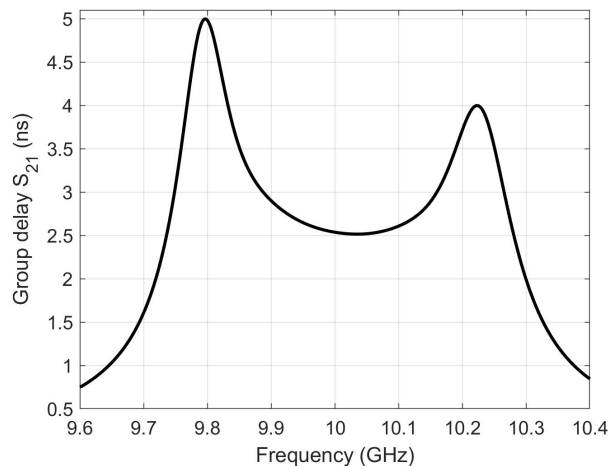
Fig. 32. Group delay of the designed dual-mode band-pass filter.

to manufacture the filter designed in Section IV-F, since its practical implementation is less complex. Furthermore, another important disadvantage of this topology compared to the filter that we have designed and manufactured, is that it is not possible to perform a manual tuning of the inductive inter-resonator coupling of the second dual-mode resonator.

V. MULTIPACTOR BREAKDOWN PREDICTION

Multipactor is an undesired phenomenon of RF breakdown affecting satellite payloads [31]. The purpose of this section is to present a rigorous study of the multipactor effect for the filter designed in Section IV-F.

First of all, we need to determine the physical areas of the filter where the multipactor effect may be expected. To do this, we will first compute the electric field in the device at the frequencies where the group delay of the filter is maximum and, next, we will identify the zones of the filter where the cited electric field is maximum. Fig. 32 shows the group delay of the S_{21} parameter of the component, where

we observe that the problematic frequencies are located at 9.797 and 10.223 GHz. However, if we recall the electrical response of the filter (see Fig. 28), we can observe that the reflected power at these frequencies is so high that the results of the multipactor discharge could not be observed. Therefore, a more practical criterion would be to perform the analysis at a pair of frequencies where S_{11} is below -15 dB, thus ensuring a proper measurement of the multipactor effect. As a consequence, the new pair of critical frequencies are chosen to be 9.827 and 10.186 GHz (see Fig. 28).

The electric field is then computed in the device at the critical frequencies. By inspecting Fig. 33, which displays the electric field calculated at 9.827 GHz, we conclude that the field is maximum in two areas: a zone surrounding the top of the re-entrant posts, and an area near the auxiliary post used to couple the two modes of the dual-mode cavities.

Next, the commercial software SPARK3D (from AuroraSat, now with CST and Dassault Systèmes) is used to estimate the multipactor power thresholds in the designed filter. In the simulations, the initial number of electrons is set at 20000, while the multipactor criterion growth factor is chosen to be equal to 10. Two different analysis have been carried out in order to check the convergence of the power thresholds that we obtained. In the first one, SPARK3D distributes the initial elec-
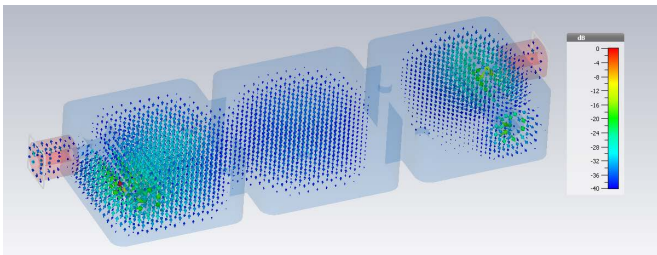
Fig. 33. Computation of the electric field in the designed filter at 9.827 GHz.
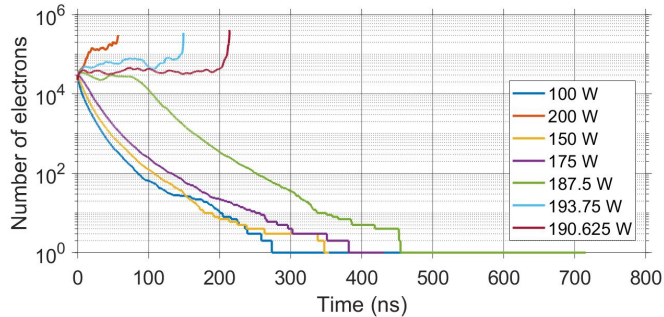

Fig. 34. Simulation of the multipactor discharge: evolution of the number of electrons in the filter calculated at $f = 10.186$ GHz.

TABLE III
POWER THRESHOLD OF THE MULTIPACTOR EFFECT

Frequency (GHz)	Power threshold (W)
9.827	135.93
10.186	189.06

trons automatically in the whole filter geometry, while in the second analysis the electrons are confined only in the critical areas of the dual-mode cavities previously described. The results obtained are essentially identical in both simulations, thus confirming the validity of the procedure. In particular, Fig. 34 shows the evolution of the number of electrons in the filter for different RF power levels calculated at $f = 10.186$ GHz. As we can see, the number of electrons grows exponentially when the corresponding multipactor power threshold is reached. Furthermore, the estimated multipactor power thresholds for each critical frequency are given in Table III. Given the values obtained, the filter we propose can indeed be used in space applications, such as the RF satellite payloads of satellite navigation and mobile communications systems, or in any other space application operating in the same frequency range.

Finally, a last simulation has been performed using a low number of electrons (i.e. 1000) in order to track their trajectory and better identify the zones where the discharge takes place at each critical frequency. The results that we have obtained confirm, as we expected, that the discharge occurs at the top of the re-entrant post for $f = 9.827$ GHz, and near the auxiliary post used to couple the two modes of the dual-mode cavities for $f = 10.186$ GHz.
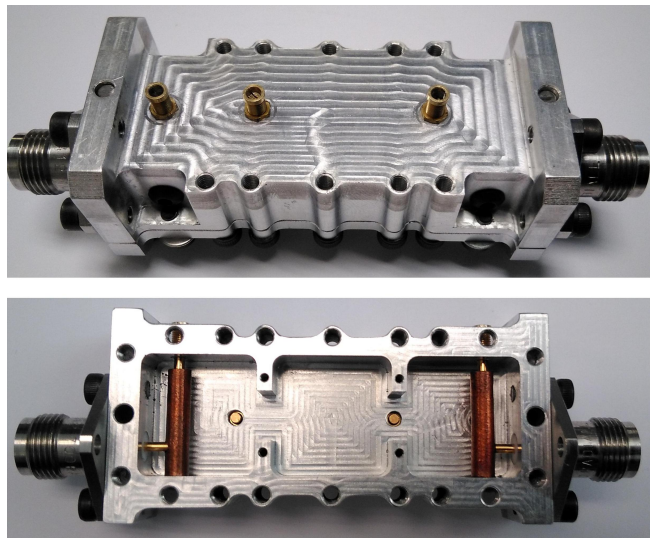
Fig. 35. Photograph of the breadboard: assembled device (up), and body without cover (down).
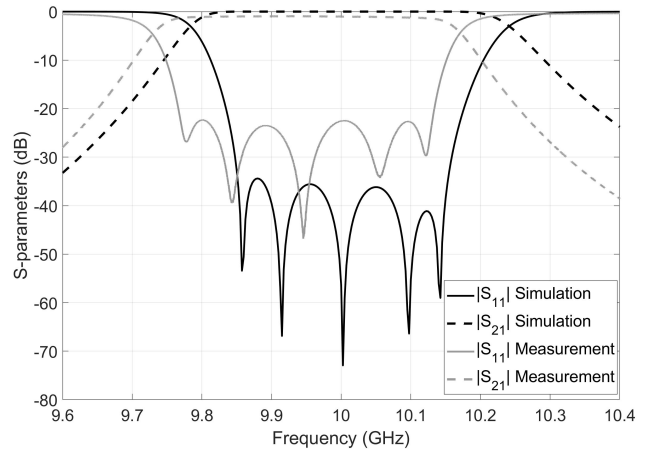
Fig. 36. Measurement of the in-band performance of the manufactured filter breadboard.

VI. PRACTICAL IMPLEMENTATION OF THE DUAL-MODE COAXIAL FILTER

In order to validate both the filter structure and the design procedure, we have fabricated and measured a filter prototype. The breadboard has been fabricated in aluminum using standard low-cost milling. Fig. 35 shows a photograph of the filter prototype, while Fig. 36 shows both the measured and simulated in-band response for the dual-mode filter designed in Section IV-F. Although an equiripple response has been indeed obtained after performing a manual tuning, we can observe that a frequency shift is still present in the measured in-band response (it is centered at 9.95 GHz). The level of return loss is also lower than expected.

To better understand the results obtained, we have measured several dimensions of the manufactured breadboard using an optical measuring machine (OGP Flash CNC 200 Multi-Sensor Coordinate Measurement System). The precision of the measuring system is within the range 3-5 μm. The results

TABLE IV
MEASUREMENT OF THE DIMENSIONS OF THE FABRICATED FILTER

Dimension	Design (mm)	Measurement (mm)	Error (μm)
a (cavity 1)	20.0	20.056	56
a (cavity 2)	20.0	20.048	48
a (cavity 3)	20.0	20.018	18
b (cavity 1)	10.0	9.989	11
b (cavity 2)	10.0	10.006	6
b (cavity 3)	10.0	9.987	13
l (cavity 1)	18.821	18.874	53
l_{er}	19.798	19.805	7
l (cavity 3)	18.821	18.862	41
h_{p1} (cavity 1)	18.0	17.963	37
h_{p1} (cavity 3)	18.0	17.931	69
R_{p1} (cavity 1)	2.0	1.951	49
R_{p1} (cavity 3)	2.0	1.964	36
l_p (cavity 1)	3.236	3.471	235
l_p (cavity 3)	3.236	3.283	47
l_c (cavity 1)	4.801	4.880	79
l_c (cavity 3)	4.801	4.852	51
t (iris 1)	2.5	2.476	24
t (iris 2)	2.5	2.485	15
a_i (iris 1)	8.092	8.164	72
a_i (iris 2)	8.092	8.151	59

Fig. 37. Measurement of the out-of-band performance of the filter breadboard.

TABLE V
EVALUATION OF THE YIELD FOR THE FILTER BREADBOARD

Tolerance	5 μm	7.5 μm	10 μm	12.5 μm
Yield	36%	10%	3%	2%

Fig. 38. Tolerance analysis of the dual-mode coaxial filter.

of the measurement are given in Table IV (the notation used for the different variables can be found in Fig. 2 and Fig. 21). As we expected, we can see that there are important manufacturing errors. We believe that these errors are the reason for the degradation of the in-band response. To further validate this conclusion, we discuss in the next section the results of a tolerance analysis.

Finally, Fig. 37 shows the out-of-band performance of the filter breadboard. The result obtained is in very good agreement with our simulations, even though the transmission zero is not visible in the experimental results due to the noise floor of the network analyzer.

VII. TOLERANCE ANALYSIS

As we mentioned already, we now discuss the results of a tolerance analysis for the filter designed in Section IV-F. For this purpose, the commercial tool FEST3D has been used adding to all dimensions a random error with a Gaussian distribution. Several simulations have been performed and the manufacturing yield has been calculated with different values for the standard deviation (± 5, ± 7.5, ± 10 and ± 12.5 μm). The threshold for the yield evaluation has been set to a value of 25 dB for the in-band return loss level. The results obtained are shown in Table V. As we can see, this structure is indeed very sensitive to manufacturing errors. The use of tuning elements is therefore mandatory in order to obtain an acceptable in-band response. It is important to note, however, that even with the help of the tuning screws, a small (acceptable) residual difference between the measurements and the ideal filter performance is still present. This is probably

due to the fact that the breadboard does not allow for the tuning of the input and output couplings. Furthermore, Fig. 38 shows a number of simulations including a random error in the dimensions of the filter. In view of all these results, we can conclude that it is very difficult to obtain satisfactory in-band responses when the manufacturing errors are above 7.5 μm. This fact, together with the manufacturing errors reported in Table IV, explains very clearly why we have not been able to recover the ideal response with the prototype that we have fabricated, even though we have used a number of tuning elements.

Tuning element	Depth (mm)
Top screw of first dual-mode cavity (h_s)	2.624
Coupling post of first dual-mode cavity (h_a)	1.719
Screw S_1 of first dual-mode cavity	1.144
Screw S_2 of first iris	1.219
Screw S_3 of empty cavity	1.279
Screw S_2 of second iris	1.234
Top screw of second dual-mode cavity (h_s)	2.649
Coupling post of second dual-mode cavity (h_a)	1.754
Screw S_1 of second dual-mode cavity	1.519

Fig. 39. Simulated response obtained for estimating the depths of the tuning elements.

VIII. ESTIMATION OF THE DEPTHS OF THE TUNING ELEMENTS IN THE FILTER BREADBOARD

To further understand the behavior of the filter structure we propose in this paper, we now discuss a systematic procedure, based on space mapping techniques, for estimating the depth at which the different tuning elements of the breadboard must be set in order to obtain the experimental result presented in Fig. 36. First of all, a high-accuracy electrical response of the real device (i.e., a filter with the physical dimensions presented in Table IV) is obtained using Ansys HFSS. In this simulation, the depth of all the tuning elements is set at the proper design value (see Section IV). For the sake of clarity, let f denote the real device, and let $R(f)$ represent the electrical response of the real device.

Next, a new filter (called f_{coarse}) with a response equal to $R(f)$ needs to be synthesized in the coarse space. To do that, we compute the difference between the real dimensions of the device and the dimensions of the filter designed in the high-accuracy space (see Section IV-F). The differences are then applied to the dimensions of the filter designed in the coarse space (see Section IV-E) to synthesize (after a slight optimization) the dimensions of the new f_{coarse} filter.

After that, we start with the iterative application of the ASM technique. In all the iterations performed, the only variables that have been optimized are the depths of the tuning elements. In the first step, the electrical response of the filter f_{coarse} is optimized considering the measured (*tuned*) response of the filter manufactured as the target function. After each iteration, the depths of the tuning elements of filter f are properly modified. At the end of this procedure, we obtain a filter in the fine space (with dimensions equal to the measured values shown in Table IV) with the appropriate tuning elements depths to produce an electrical response similar (*ideally identical*) to the one of the filter that we have manufactured. Fig. 39 shows a comparison between the measured performance of the filter and the simulated response in the fine space, after 10 ASM iterations. As we can see, an acceptable agreement has indeed been obtained. The estimated values for the depth of the tuning screws are given in Table VI (the notation used to identify the tuning elements can be found in Fig. 15 and Fig. 26).

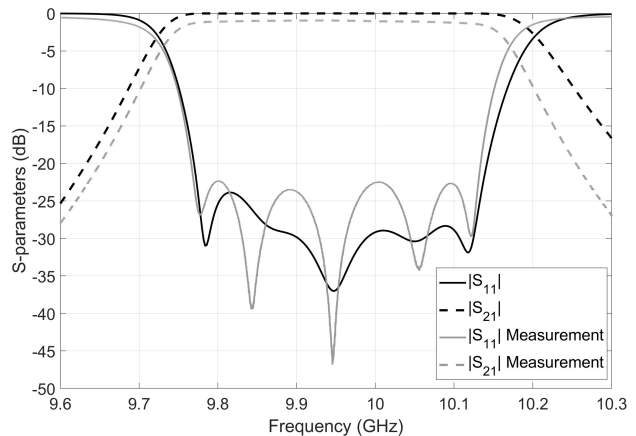Finally, it is interesting to note that the procedure just described can also be effectively used to support the manual tuning of the filter, as discussed in [32].

IX. CONCLUSION

In this contribution, we have presented a band-pass filter structure based on a novel dual-mode resonator. The novel dual-mode resonator is obtained integrating a coaxial resonator in a rectangular waveguide cavity (the housing). The filter has been designed following a systematic step-by-step procedure based on the use of equivalent circuits. Mechanization effects have also been taken into account during the design process. The design strategy has been validated through the fabrication and measurement of a filter prototype. The measured filter performance is found to be in reasonable agreement with the ideal response, even though some discrepancies have been identified. However, the discrepancies have been fully justified with a rigorous tolerance analysis, thereby fully validating both the novel filter structure proposed and the complete design process.

REFERENCES

[1] G. L. Matthaei, "Comb-line band-pass filters of narrow or moderate bandwidth," *Microw. J.*, vol. 6, p. 82–91, Aug. 1963.

[2] P. Vallerotonda, L. Pelliccia, C. Tomassoni, F. Cacciamani, R. Sorrentino, J. Galdeano, and C. Ernst, "Compact waveguide bandpass filters for broadband space applications in C and Ku-bands," in *Proc. 1st Eur. Microw. Conf. Central Europe*, May 2019, pp. 116–119.

[3] K. Kobrin, V. Rudakov, V. Sledkov, L. Zimeng, and M. Manuilov, "A novel design of wideband diplexer for base station applications," in *Proc. Radiat. Scattering Electromagn. Waves*, Jun. 2019, pp. 148–151.

[4] Z. Li, P. Zhao, and K. Wu, "An I/O coupling multiplier circuit and its application to wideband filters and diplexers," *IEEE Trans. Compon. Packag. Manuf. Technol.*, vol. 8, no. 5, pp. 858–866, May 2018.

[5] C. Tomassoni, L. Pelliccia, F. Cacciamani, P. Vallerotonda, R. Sorrentino, J. Galdeano, and C. Ernst, "Compact broadband waveguide filter with wide spurious-free range based on mixed TM and combline resonators," in *Proc. 47th Eur. Microw. Conf.*, Oct. 2017, pp. 985–988.

[6] A. V. G. Subramanyam, D. Sivareddy, V. V. Srinivasan, and V. K. Hariharan, "Multipaction-free combline diplexer for deep space applications," in *Proc. IEEE Int. Microw. RF Conf.*, Dec. 2014, pp. 217–220.

[7] X. Wang, Q. Wang, Y. Zhao, and H. Li, "Design of a compact diplexer," in *IEEE MTT-S Int. Microw. Workshop Ser. Art of Miniaturizing RF Microw. Passive Compon.*, Dec. 2008, pp. 170–172.

[8] A. Abramowicz, "Method for cross couplings realization in comb-line filters," in *Int. Conf. Electromagn. Adv. Appl.*, Sep. 2019, pp. 1074–1075.

[9] A. S. Rong, H. Yang, X. H. Chen, and A. Cangellaris, "Efficient FDTD modeling of irises/slots in microwave structures and its application to the design of combline filters," *IEEE Trans. Microw. Theory Techn.*, vol. 49, no. 12, pp. 2266–2275, Dec. 2001.

[10] M. El Sabbagh, K. A. Zaki, Hui-Wen Yao, and M. Yu, "Full-wave analysis of coupling between combline resonators and its application to combline filters with canonical configurations," *IEEE Trans. Microw. Theory Techn.*, vol. 49, no. 12, pp. 2384–2393, Dec. 2001.

[11] H. Yao, K. A. Zaki, A. E. Atia, and R. Hershtig, "Full wave modeling of conducting posts in rectangular waveguides and its applications to slot coupled combline filters," *IEEE Trans. Microw. Theory Techn.*, vol. 43, no. 12, pp. 2824–2830, Dec. 1995.

[12] M. Hoft, S. Burger, T. Magath, and O. Bartz, "Compact combline filter with improved cross coupling assembly and temperature compensation," in *Proc. Asia–Pacific Microw. Conf.*, Dec. 2006, pp. 781–784.

[13] C. Wang and K. A. Zaki, "Full-wave modeling of electric coupling probes in comb-line resonators and filters," *IEEE Trans. Microw. Theory Techn.*, vol. 48, no. 12, pp. 2459–2464, Dec. 2000.

[14] Y. Wang and M. Yu, "True inline cross-coupled coaxial cavity filters," *IEEE Trans. Microw. Theory Techn.*, vol. 57, no. 12, pp. 2958–2965, Dec. 2009.

[15] G. Macchiarella, M. Santoniccolo, M. Fumagalli, and A. Sartorio, "Combline filters using conical resonators," in *Proc. 33rd Eur. Microw. Conf.*, vol. 1, Oct. 2003, pp. 167–169.

[16] Q. H. Li and K. M. Cheng, "A novel resonator filter configuration with cellular-liked structure," in *Proc. Asia–Pacific Microw. Conf.*, vol. 5, Dec. 2005, pp. 1–4.

[17] R. Tkadlec and G. Macchiarella, "Pseudoelliptic combline filter in a circularly shaped tube," in *IEEE MTT-S Int. Microw. Symp. Dig.*, Jun. 2018, pp. 1099–1102.

[18] D. Sh-Asanjan and R. R. Mansour, "A novel coaxial resonator for high power applications," in *Proc. 44th Eur. Microw. Conf.*, Oct. 2014, pp. 295–298.

[19] J. S. Parish, N. Somjit, and I. C. Hunter, "Continuous frequency and bandwidth tunable combline cavity bandpass filters with internally mounted motors," *IET Microw. Antennas Propag.*, vol. 12, no. 15, pp. 2332–2337, 2018.

[20] S. Kurudere and V. B. Ertürk, "Novel microstrip fed mechanically tunable combline cavity filter," *IEEE Microw. Wireless Compon. Lett.*, vol. 23, no. 11, pp. 578–580, Nov. 2013.

[21] H. Chen, R. Hsieh, Y. Shih, Y. Chou, and M. Chen, "Coaxial combline filters using the stepped-impedance resonators," in *Proc. Asia–Pacific Microw. Conf.*, Dec. 2010, pp. 1724–1727.

[22] M. A. Ismail, D. Smith, A. Panariello, Y. Wang, and M. Yu, "EM-based design of large-scale dielectric-resonator filters and multiplexers by space mapping," *IEEE Trans. Microw. Theory Techn.*, vol. 52, no. 1, pp. 386–392, Jan. 2004.

[23] A. A. San-Blas, J. Pérez-Guijarro, V. E. Boria, and M. Guglielmi, "Systematic procedure for the efficient design of folded waveguide comb-line filters," in *IEEE MTT-S Int. Conf. Numer. Electromagn. Multiphys. Model. Optim.*, May 2019, pp. 1–4.

[24] A. Morini, G. Venanzoni, M. Farina, and T. Rozzi, "Modified adaptive prototype inclusive of the external couplings for the design of coaxial filters," *IEEE Trans. Microw. Theory Techn.*, vol. 55, no. 9, pp. 1905–1911, Sep. 2007.

[25] J. A. Ruiz-Cruz, M. M. Fahmi, and R. R. Mansour, "Dual-resonance combline resonator for dual-band filters," in *IEEE MTT-S Int. Microw. Symp. Dig.*, Jun. 2012, pp. 1–3.

[26] ——, "Triple-conductor combline resonators for dual-band filters with enhanced guard-band selectivity," *IEEE Trans. Microw. Theory Techn.*, vol. 60, no. 12, pp. 3969–3979, Dec. 2012.

[27] A. A. San Blas, J. C. Melgarejo, V. E. Boria, and M. Guglielmi, "Novel solution for the coaxial excitation of inductive rectangular waveguide filters," in *Proc. 48th Eur. Microw. Conf.*, Sep. 2018, pp. 89–92.

[28] J. W. Bandler, R. M. Biernacki, Shao Hua Chen, R. H. Hemmers, and K. Madsen, "Electromagnetic optimization exploiting aggressive space mapping," *IEEE Trans. Microw. Theory Techn.*, vol. 43, no. 12, pp. 2874–2882, Dec. 1995.

[29] K. L. Wu, R. R. Mansour, and H. Wang, "A full wave analysis of a conductor post insert reentrant coaxial resonator in rectangular waveguide combline filters," in *IEEE MTT-S Int. Microw. Symp. Dig.*, vol. 3, Jun. 1996, pp. 1639–1642.

[30] G. L. Matthaei, L. Young, and E. M. T. Jones, *Microwave Filters, Impedance-Matching Networks and Coupling Structures*. Artech House, 1980.

[31] J. R. M. Vaughan, "Multipactor," *IEEE Trans. Electron Devices*, vol. 35, no. 7, pp. 1172–1180, Jul. 1988.

[32] J. C. Melgarejo, J. Ossorio, S. Cogollos, M. Guglielmi, V. E. Boria, and J. W. Bandler, "On space mapping techniques for microwave filter tuning," *IEEE Trans. Microw. Theory Techn.*, vol. 67, no. 12, pp. 4860–4870, Dec. 2019.

Ángel Antonio San-Blas was born in Fortaleny (Valencia), Spain, in 1976. He received the Ingeniero de Telecomunicación degree and the Doctor Ingeniero de Telecomunicación degree from the Universitat Politècnica de València, Valencia, Spain, in 2000 and 2008, respectively.

In 2001 and 2002, he was a Researcher Assistant with the Departamento de Comunicaciones, Universitat Politècnica de València, where he was involved in the development of simulation tools for the analysis and design of waveguide devices. From November 2001 to March 2002, he hold a researcher position with the Department of Electronics at the Università degli Studi di Pavia, Pavia, Italy, involved in the research project "Millimeter-Wave and Microwave Components Design Framework for Ground and Space Multimedia Network" (V European Framework Project).

Since 2003, he has been an Associate Professor at the Departamento de Ingeniería de Comunicaciones, Universidad Miguel Hernández de Elche, Elche, Spain. Furthermore, he currently serves as an Editorial Board Member (Area Editor) for the International Journal of Electronics and Communications (Elsevier). His current research interests include the analysis and design of passive waveguide components for satellite communication systems.

Marco Guglielmi (F'13) was born in Rome, Italy, in 1954. He received the Laurea degree in ingegneria elettronica from the University of Rome La Sapienza, Rome, Italy, in 1979, where he attended the Scuola di Specializzazione in Elettromagnetismo Applicato in 1980, the M.S. degree in electrical engineering from the University of Bridgeport, Bridgeport, CT, USA, in 1982, and the Ph.D. degree in electrophysics from Polytechnic University, Brooklyn, NY, USA, in 1986.

From 1984 to 1986, he was an Academic Associate with Polytechnic University, where he was an Assistant Professor from 1986 to 1988. From 1988 to 1989, he was an Assistant Professor with the New Jersey Institute of Technology, Newark, NJ, USA. In 1989, he joined the European Space Agency as a Senior Microwave Engineer with the RF System Division, European Space Research and Technology Centre (ESTEC), Noordwijk, The Netherlands, where he was in charge of the development of microwave filters and electromagnetic simulation tools. In 2001, he was appointed as the Head of the Technology Strategy Section of ESTEC, where he contributed to the development of management processes and tools for the formulation of a European strategy for Space Technology Research and Development. In 2014, he retired from the European Space Agency and is currently holding the position of Invited Senior Researcher at the Universitat Politècnica de València, Valencia, Spain.

Dr. Guglielmi was elevated to the grade of Fellow of the IEEE in January 2013 for contributions to multimode equivalent networks and microwave filter design. In 1981, he was a recipient of the Fulbright Scholarship, Rome, Italy, and the Halsey International Scholarship Programme (HISP) from the University of Bridgeport.

Juan Carlos Melgarejo was born in Alicante, Spain in 1993. He obtained his bachelor's degree in Telecommunications Engineering from the Universitat Politècnica de València (UPV), Valencia, Spain, in 2015. He continued his studies with the UPV, where he obtained a double Master in Telecommunications Systems in 2019. Currently, he is pursuing his Ph.D. at the UPV, and his main research interests are focused on microwave passive devices and new manufacturing techniques for satellite components.

Ángela Coves (S'04–M'05–SM'19) received the Licenciado and Doctor degrees in Physics from the Universitat de València, Valencia, Spain. She is an Associate Professor at Universidad Miguel Hernández de Elche, Elche, Spain. Her research interests are focused on microwave passive components and RF breakdown high-power effects.

Vicente E. Boria (S'91-A'99-SM'02-F'18) was born in Valencia, Spain, on May 18, 1970. He received his Ingeniero de Telecomunicación degree (with first-class honors) and the Doctor Ingeniero de Telecomunicación degree from the Universitat Politècnica de València, Valencia, Spain, in 1993 and 1997, respectively.

In 1993 he joined the Departamento de Comunicaciones, Universitat Politècnica de València, where he has been Full Professor since 2003. In 1995 and 1996, he was holding a Spanish Trainee position with the European Space Research and Technology Centre, European Space Agency (ESTEC-ESA), Noordwijk, The Netherlands, where he was involved in the area of EM analysis and design of passive waveguide devices. He has authored or co-authored 15 chapters in technical textbooks, 180 papers in refereed international technical journals, and over 200 papers in international conference proceedings. His current research interests are focused on the analysis and automated design of passive components (in particular filters and multiplexers) in several technologies, as well as on the simulation and measurement of power effects in high-frequency devices and systems.

Dr. Boria has been a member of the IEEE Microwave Theory and Techniques Society (IEEE MTT-S) and the IEEE Antennas and Propagation Society (IEEE AP-S) since 1992. He is also member of the European Microwave Association (EuMA), and has been the Chair of the 48th European Microwave Conference held in Madrid, Spain. He acts as a regular reviewer of the most relevant IEEE and IET technical journals on his areas of interest. He has been Associate Editor of IEEE Microwave and Wireless Components Letters (2013-2018) and IET Electronics Letters (2015-2018). Presently, he serves as Subject Editor (Microwaves) of IET Electronics Letters, and as Editorial Board member of International Journal of RF and Microwave Computer-Aided Engineering. He is also member of the Technical Committees of the IEEE-MTT International Microwave Symposium and of the European Microwave Conference.